JOURNAL OF AIRCRAFT
Vol. 40, No. 2, March–April 2003

Parametric Study of Flutter for an Airfoil in Inviscid Transonic Flow

Denis B. Kholodar,* Jeffrey P. Thomas,† Earl H. Dowell,‡ and Kenneth C. Hall§
Duke University, Durham, North Carolina 27708-0300

With the use of a state of the art inviscid computational fluid dynamic harmonic balance aerodynamic-Euler-based code, a systematic, parametric investigation is presented into how the several structural parameters and freestream Mach number of a transonic flow affect the flutter characteristics of a "typical" two-degree-of-freedom transonic airfoil configuration. The computational efficiency of the time-linearized option of the harmonic balance aerodynamic model allows a much more thorough exploration of the parameter range than has been possible previously.

Nomenclature

a	=	nondimensional location of airfoil elastic axis, e/b
b, c	=	semichord and chord, respectively
$\bar{c}_l, \bar{c}_m$	=	first harmonic coefficient of lift and moment about elastic axis, respectively
$\bar{c}_{l_{\bar{h}}}, \bar{c}_{l_{\bar{\alpha}}}$	=	first harmonic coefficient of lift due to plunge and pitch motions, respectively
$\bar{c}_{m_{\bar{h}}}, \bar{c}_{m_{\bar{\alpha}}}$	=	first harmonic coefficient of moment due to plunge and pitch motions, respectively
e	=	location of airfoil elastic axis, measured positive aft of airfoil midchord
h, α	=	airfoil plunge and pitch degree of freedom (DOF), respectively
h_{av}	=	averaged grid step in the radial direction, identical to $(R/c - \frac{1}{2})/(N_r - 1)$
$\bar{h}, \bar{\alpha}$	=	first harmonic amplitude of plunge nondimesionalized by semichord, $\bar{h}$ is equal to h/b, and pitch motion, respectively
I_α	=	second moment of inertia about elastic axis
K_h, K_α	=	airfoil plunge stiffness and torsional stiffness about elastic axis, respectively
k	=	reduced frequency based on airfoil semichord, identical to $\omega b/U_\infty$
L, M_{ea}	=	lift and moment about elastic axis, respectively
M	=	freestream Mach number
m	=	airfoil sectional mass
N	=	number of harmonics used in harmonic balance solver
N_r, N_Θ	=	number of grid points in radial and circumferential direction, respectively
R	=	radius of computational domain
r_α	=	radius of gyration of airfoil about elastic axis, r_α^2 is identical to I_α/mb^2
S_α	=	first moment of inertia about elastic axis
U_∞	=	freestream velocity
V	=	reduced velocity, identical to $U_\infty/\omega_\alpha b$
$V_f/\sqrt{\mu}$	=	flutter speed index, $U_{\infty f}/\sqrt{\mu}\omega_\alpha b$
x_α	=	airfoil static unbalance, S_α/mb
μ	=	mass ratio, identical to $m/\pi\rho_\infty b^2$
$\omega, \bar{\omega}$	=	frequency and reduced frequency based on airfoil chord, $\bar{\omega}$ is identical to $\omega c/U_\infty$
ω_α, ω_h	=	uncoupled natural frequencies of pitch and plunge DOF
ω_1, ω_2	=	coupled structural natural frequencies

Subscript

f	=	flutter onset condition

Received 12 June 2001; revision received 27 September 2002; accepted for publication 5 October 2002.

*Research Associate, Department of Mechanical Engineering and Materials Science. Member AIAA.
†Research Assistant Professor, Department of Mechanical Engineering and Materials Science. Member AIAA.
‡J. A. Jones Professor, Department of Mechanical Engineering and Materials Science; Director, Center for Nonlinear and Complex Systems; and Dean Emeritus, School of Engineering. Fellow AIAA.
§Professor and Chairman, Department of Mechanical Engineering and Materials Science. Associate Fellow AIAA.

Introduction

TRANSONIC flow flutter and limit-cycle oscillations (LCO) are of significant interest in wing and aircraft design. The large expense incurred in both time- and frequency-domain transonic aerodynamic computations is the principal obstacle to the aeroelastician in obtaining a deeper understanding of these phenomena through a systematic parameter study.

Reduced-order modeling (ROM) techniques have been developed and used to overcome this obstacle in recent work on this subject. For a general review of the latest studies involving ROM-based methods, see Ref. 1. Padé approximants of transfer functions and various other rational polynomial curve fitting techniques also have been used in recent years for linear flutter analysis, for example, see Refs. 2–4.

In the past few years at Duke University, a number of computational fluid dynamics (CFD) time (dynamically) linearized codes have been developed[5,6] and converted to the frequency domain. ROM techniques have then been applied to these dynamically linearized CFD codes and then used for flutter analyses that are very computationally efficient.

Recently, a novel nonlinear harmonic balance (HB) method that extends the frequency domain CFD models to the fully dynamically nonlinear range has been developed. This method enables one to model efficiently nonlinear unsteady aerodynamic behavior corresponding to finite amplitude structural motion of a prescribed frequency, which can be subsequently used for modeling LCO behavior.[5–7] We believe these two methods, ROM-based flutter analysis and HB-based LCO modeling, will significantly advance the aeroelastician's capability to do rapid parametric studies.

In the current study, a time-linearized option of the Euler HB model is used to capture the effects of the mean position of the shock and small shock motions about this mean position on transonic flutter. The shock motion is assumed linearly proportional to the airfoil motion in this study.

This study also had another goal, that is, finding a (flutter) boundary of neutrally stable points for further use in a subsequent LCO

study[7] of the same model with large shock motion aerodynamic nonlinearities included.

Results for the flutter boundary using the present methodology for the famous Isogai typical section case have been discussed in Ref. 8, and a favorable comparison has been made with the results of other investigators who used potential or Euler flow models. Further comparisons with results of others from theory and experiment are included in this paper.

Governing Equations

Consider a "typical" two-degrees-of-freedom (DOF) airfoil section as shown in Fig. 1. The equations of motion of this aeroelastic system can be written in the form

$$m\ddot{h} + S_\alpha \ddot{\alpha} + K_h h = -L, \qquad S_\alpha \ddot{h} + I_\alpha \ddot{\alpha} + K_\alpha \alpha = M_{\text{ea}} \tag{1}$$

Here the left-hand-side terms represent a linear structural model approximation for the plunge and pitch coordinates. The right-hand-side terms represent the aerodynamic loading terms, which for this study are based on the HB approach applied to a discrete CFD model of the inviscid Euler equations. Here we present a summary of the method. For a more detailed description see Refs. 5 and 6.

In integral form, the unsteady Euler equations may be written as

$$\frac{\partial}{\partial t}\iint_{D(t)} \boldsymbol{U}\,\mathrm{d}D + \oint_{\partial D(t)} \left(\boldsymbol{F}(\boldsymbol{U}) - \boldsymbol{U}\frac{\partial f}{\partial t}\right)\mathrm{d}y - \oint_{\partial D(t)} \left(\boldsymbol{G}(\boldsymbol{U}) - \boldsymbol{U}\frac{\partial g}{\partial t}\right)\mathrm{d}x = 0 \tag{2}$$

where x and y are the Cartesian coordinates, t is time, and D is a deforming control volume bounded by the control surface ∂D. The quantities $\partial f/\partial t$ and $\partial g/\partial t$ are the x and y components of the velocity of the control surface ∂D. The conservation fluid variables $\boldsymbol{U}$ and flux vectors $\boldsymbol{F}$ and $\boldsymbol{G}$ are given by

$$\begin{aligned} \boldsymbol{U} &= \{\rho, \rho u, \rho v, E\}^T \\ \boldsymbol{F}(\boldsymbol{U}) &= \{\rho u, \rho u^2 + p, \rho uv, (E+p)u\}^T \\ \boldsymbol{G}(\boldsymbol{U}) &= \{\rho v, \rho uv, \rho v^2 + p, (E+p)v\}^T \end{aligned} \tag{3}$$

where ρ is the density, u and v are the velocity components in the x and y directions, respectively, p is the pressure, and E is the total energy, which is the sum of the internal and kinetic energy:

$$E = \rho e + (\rho/2)(u^2 + v^2) \tag{4}$$

Considering a calorically perfect gas, the system of equations is completed via

$$p = (\gamma - 1)\{E - (\rho/2)[u^2 + v^2]\} \tag{5}$$

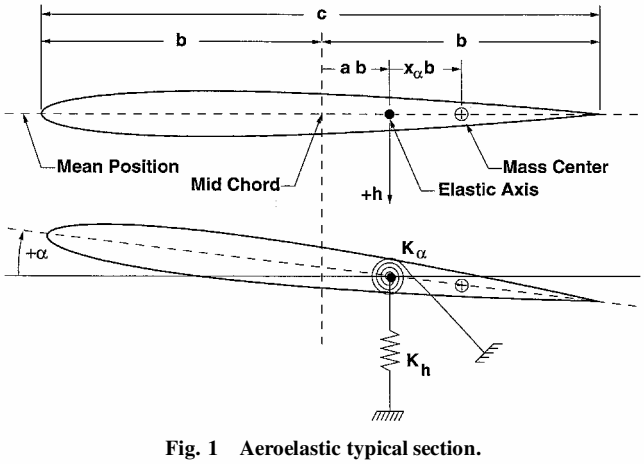

Fig. 1 Aeroelastic typical section.

Frequency-Domain Equations

The next step in the HB development is to consider strictly periodic unsteady flows of a fundamental frequency ω. The flow variables and flux vectors are then approximated using truncated Fourier series in time with spatially varying coefficients. For instance,

$$\iint_{D(t)} \boldsymbol{U}\,\mathrm{d}D \approx \sum_{n=-N}^{N} \bar{\boldsymbol{U}}_n e^{in\omega t} \tag{6}$$

and

$$\oint_{\partial D(t)} \left(\boldsymbol{F}(\boldsymbol{U}) - \boldsymbol{U}\frac{\partial f}{\partial x}\right)\mathrm{d}y - \oint_{\partial D(t)} \left(\boldsymbol{G}(\boldsymbol{U}) - \boldsymbol{U}\frac{\partial g}{\partial y}\right)\mathrm{d}x \approx \sum_{n=-N}^{N} \bar{\boldsymbol{F}}_n e^{in\omega t} \tag{7}$$

where N is the number of harmonics used in the Fourier expansion. The time derivative of the vector of conservation fluid variables is then

$$\frac{\partial}{\partial t}\iint_{D(t)} \boldsymbol{U}\,\mathrm{d}D \approx in\omega \sum_{n=-N}^{N} \bar{\boldsymbol{U}}_n e^{in\omega t} \tag{8}$$

Substituting Eqs. (7) and (8) into the Euler equations (2), multiplying by $e^{-im\omega t}$, and integrating over one period yields a system of equations for the Fourier coefficients,

$$\boldsymbol{A}\bar{\boldsymbol{U}} + \bar{\boldsymbol{F}} = 0 \tag{9}$$

where the diagonal matrix $\boldsymbol{A}$ and vectors $\bar{\boldsymbol{U}}$ and $\bar{\boldsymbol{F}}$ are

$$\begin{aligned} \operatorname{diag}\boldsymbol{A} &= \{-iN, -i(N-1), \ldots, iN\} \\ \bar{\boldsymbol{U}} &= \{\bar{\boldsymbol{U}}_{-N}, \bar{\boldsymbol{U}}_{-(N-1)}, \ldots, \bar{\boldsymbol{U}}_N\}^T \\ \bar{\boldsymbol{F}} &= \{\bar{\boldsymbol{F}}_{-N}, \bar{\boldsymbol{F}}_{-(N-1)}, \ldots, \bar{\boldsymbol{F}}_N\}^T \end{aligned} \tag{10}$$

As demonstrated by Hall et al.,[5] via a Fourier transform matrix $\boldsymbol{E}$ one can relate the Fourier coefficient variables $\bar{\boldsymbol{U}}$ to the solution variables at $(2N+1)$ discrete time levels within a period of motion. Hall et al.[5] also showed how one can express the Fourier flux coefficients in terms of time-domain flux term variables. This enables the HB methodology to be easily implemented within an existing steady CFD flow solver method. If one defines

$$\hat{\boldsymbol{U}} \equiv \begin{Bmatrix} \hat{U}(t_0) \\ \cdots \\ \hat{U}(t_N) \end{Bmatrix} \equiv \begin{Bmatrix} \displaystyle\iint_{D(t_0)} \boldsymbol{U}(t_0)\,\mathrm{d}D \\ \cdots \\ \displaystyle\iint_{D(t_N)} \boldsymbol{U}(t_N)\,\mathrm{d}D \end{Bmatrix} \tag{11}$$

and

$$\hat{\boldsymbol{F}} \equiv \begin{Bmatrix} \boldsymbol{F}(t_0) \\ \cdots \\ \boldsymbol{F}(t_N) \end{Bmatrix} \equiv \begin{Bmatrix} \displaystyle\oint_{\partial D(t_0)} \left(\boldsymbol{F}(\boldsymbol{U}) - \boldsymbol{U}\frac{\partial f}{\partial x}\right)\Big|_{t_0} \mathrm{d}y - \oint_{\partial D(t_0)} \left(\boldsymbol{G}(\boldsymbol{U}) - \boldsymbol{U}\frac{\partial g}{\partial y}\right)\Big|_{t_0} \mathrm{d}x \\ \cdots \\ \displaystyle\oint_{\partial D(t_N)} \left(\boldsymbol{F}(\boldsymbol{U}) - \boldsymbol{U}\frac{\partial f}{\partial x}\right)\Big|_{t_N} \mathrm{d}y - \oint_{\partial D(t_N)} \left(\boldsymbol{G}(\boldsymbol{U}) - \boldsymbol{U}\frac{\partial g}{\partial y}\right)\Big|_{t_N} \mathrm{d}x \end{Bmatrix} \tag{12}$$

where

$$t_n = \frac{2\pi n}{(2N+1)\omega}, \qquad n = 0, 1, \ldots, 2N \tag{13}$$

then

$$\bar{\boldsymbol{U}} = \boldsymbol{E}\hat{\boldsymbol{U}}, \qquad \bar{\boldsymbol{F}} = \boldsymbol{E}\hat{\boldsymbol{F}} \tag{14}$$

Substituting Eqs. (14) into the equation for the Fourier coefficients, Eq. (9), yields

$$\boldsymbol{AE}\hat{\boldsymbol{U}} + \boldsymbol{E}\hat{\boldsymbol{F}} = 0 \tag{15}$$

which after premultiplying by $\boldsymbol{E}^{-1}$ results in

$$\boldsymbol{D}\hat{\boldsymbol{U}} + \hat{\boldsymbol{F}} = 0 \tag{16}$$

where $\boldsymbol{D} \equiv \boldsymbol{E}^{-1}\boldsymbol{AE}$ is the spectral source term operator that represents and approximates the temporal partial derivative, $\partial/\partial t$. As noted in Refs. 5 and 6, to solve the harmonic balance equations, one can add a pseudotime-derivativeterm $\partial\hat{\boldsymbol{U}}/\partial\tau$ to Eq. (16),

$$\frac{\partial\hat{\boldsymbol{U}}}{\partial\tau} + \boldsymbol{D}\hat{\boldsymbol{U}} + \hat{\boldsymbol{F}} = 0 \tag{17}$$

where τ is a fictitious time. Because only a "steady-state," temporally periodic solution is desired, local time-stepping and multiple-grid acceleration techniques can be used to increase the speed of computational convergence. The described procedures allow one to model nonlinear unsteady aerodynamic of a prescribed frequency very efficiently. Again, see Refs. 5 and 6 for additional details.

Computational Model

Figure 2a shows the O-type computational grid used; a closeup in Fig. 2b shows the grid cells that surround a symmetric NACA 64A010A airfoil. The mesh consists of $N_r \times N_\Theta$ radial and circumferential nodes. Flutter results presented in this paper are computed using either 65×65 or 97×97 grids. However, grids of 25×25, 33×33, 49×49, and 129×129 were also considered for a grid convergence study. The outer boundary radius or domain radius R was chosen to be either 5 or 10 chord lengths; however, the domains of $R/c = 15$ and 20 chord lengths were also considered. The dependence of the calculated aerodynamic forces and flutter boundaries on the grid and domain size was investigated to ensure convergence of the numerical results. A slight variant of the standard node-centered Lax–Wendroff scheme was used to solve the Euler equations. See Refs. 9 and 10 for further details.

Convergence Study Results

The dependence of the calculated aerodynamic forces on the grid and domain size was investigated for Mach numbers of $M = 0.7$ and 0.8 for various values of the reduced frequency.

In the case of the grid size, it was found that the variation of aerodynamic forces is monotonic and "close to linear" when plotted vs a squared measure of grid spacing. This is what one would desire because the CFD code used is a second-order model in the spatial variables. The dependence of the aerodynamic forces on the domain size, however, is not monotonic. Shown in Figs. 3 and 4 are the dependence of the flutter boundaries on the grid and domain size, respectively. In Fig. 3, the flutter speed index and reduced frequency appear to be nearly linear functions of the grid step. Moreover, noting the magnified scales of the vertical axes, one can conclude that flutter results (for these Mach numbers) are weakly influenced by the grid size. The flutter results in Fig. 4 show that increasing the domain size from $R/c = 5$ does not lead to substantial changes in the flutter velocity index or frequency. For more results on grid and domain convergence, see Ref. 11.

Aerodynamic Lift and Moment

For a simple harmonic motion of the airfoil,

$$h/b = \bar{h}e^{i\omega t}, \qquad \alpha = \bar{\alpha}e^{i\omega t} \tag{18}$$

the aerodynamic forces will usually be periodic in time, and for aeroelastic analysis the first harmonic will be dominant. Thus, to a good approximation,

$$L = \left(\rho U_\infty^2 c/2\right)\bar{c}_l e^{i\omega t}, \qquad M_{\text{ea}} = \left(\rho U_\infty^2 c^2/2\right)\bar{c}_m e^{i\omega t} \tag{19}$$

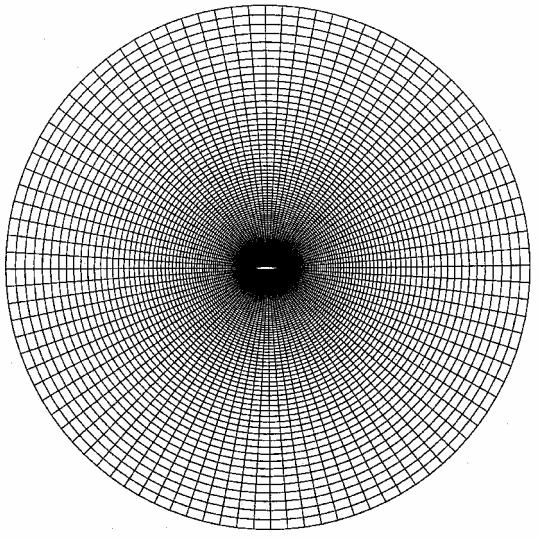

a) Overall view

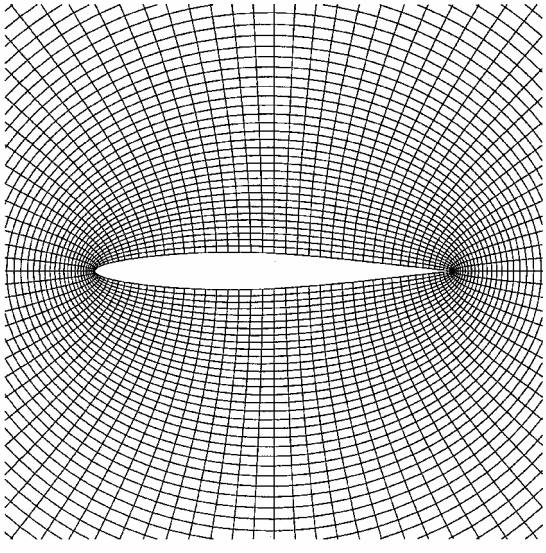

b) Closeup

Fig. 2 CFD 97×97 grid with outer boundary radius of 10-chord lengths around NACA 64A010A airfoil.

In general, the nondimensional lift and moment coefficients are expressed as

$$\begin{aligned} \bar{c}_l &= \bar{c}_l(\bar{\omega},\ \text{geometry},\ M, \bar{h}, \bar{\alpha}) \\ \bar{c}_m &= \bar{c}_m(\bar{\omega},\ \text{geometry}, M, \bar{h}, \bar{\alpha}) \end{aligned} \tag{20}$$

where $\bar{c}_l$ and $\bar{c}_m$ are nonlinear functions of $\bar{h}$ and $\bar{\alpha}$. However, in dynamically or time-linearized aerodynamics (used in flutter analyses per se), the nondimensional lift and moment coefficients are linearly proportional to $\bar{h}$ and $\bar{\alpha}$:

$$\begin{aligned} \bar{c}_l &= \bar{c}_{l_{\bar{h}}}(\bar{\omega},\ \text{geom},\ M)\bar{h} + \bar{c}_{l_{\bar{\alpha}}}(\bar{\omega},\ \text{geom},\ M)\bar{\alpha} \\ \bar{c}_m &= \bar{c}_{m_{\bar{h}}}(\bar{\omega},\ \text{geom},\ M)\bar{h} + \bar{c}_{m_{\bar{\alpha}}}(\bar{\omega},\ \text{geom},\ M)\bar{\alpha} \end{aligned} \tag{21}$$

Note that $\bar{c}_{l_{\bar{\alpha}}} \equiv \bar{c}_l/\bar{\alpha}$ for $\bar{h} \equiv 0$, as $\bar{\alpha} \to 0\ \bar{c}_{l_{\bar{\alpha}}} = \mathrm{d}\bar{c}_l/\mathrm{d}\bar{\alpha}|\bar{\alpha} = 0$. Similar definitions hold for $\bar{c}_{l_{\bar{h}}}$, $\bar{c}_{m_{\bar{h}}}$, and $\bar{c}_{m_{\bar{\alpha}}}$. For reference purposes, the case of zero Mach number was considered as well. The closed-form expressions[11] for the lift and moment coefficients due to the pitch and plunge motion were obtained from the classical Theodorsen's formulas.

Some representative results for linear aerodynamic behavior computed by running the HB aerodynamic solver with very small amplitude motion ($h = 0.001$) are presented in Fig. 5, which shows the real and imaginary parts of the aerodynamic moment due to the

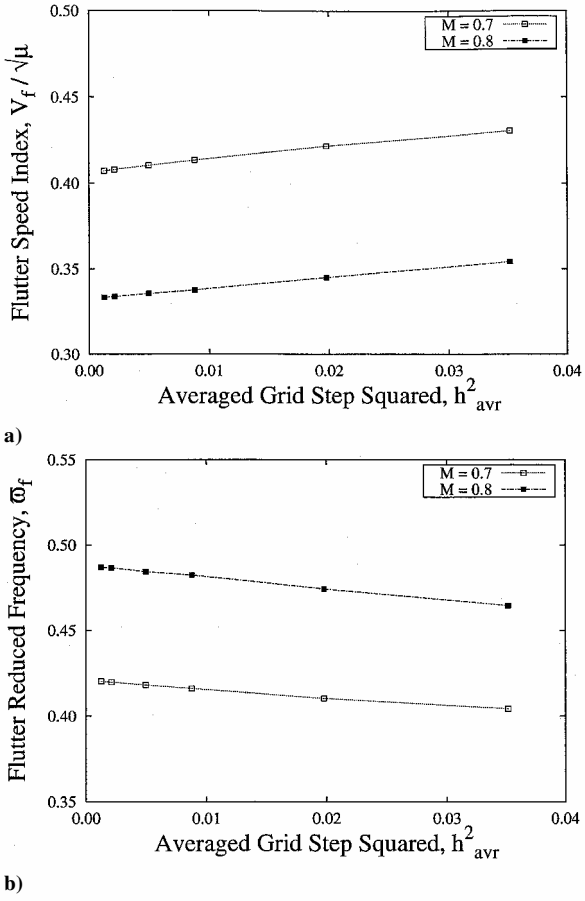

Fig. 3 Squared value of averaged grid step for Meshes $N \times N$ of $N = 129, 97, 65, 49, 33$, and 25 vs a) flutter speed index and b) reduced frequency.

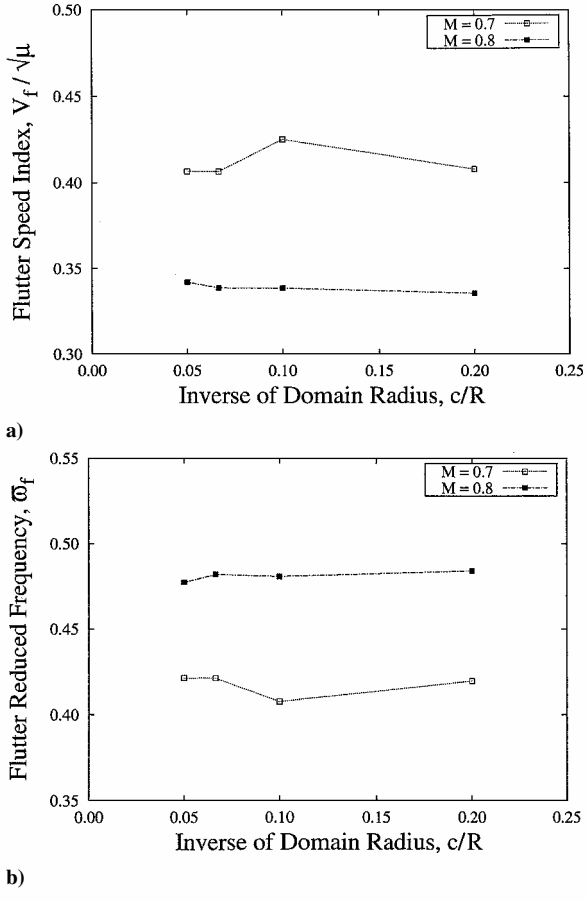

Fig. 4 Domain radius vs a) flutter speed index and b) reduced frequency.

plunge motion, $\bar{c}_{m_{\bar{h}}}$, vs reduced frequency. This (symmetric NACA 64A010A) airfoil has a strong shock in the range of $0.8 < M < 0.9$. For subsonic Mach numbers $0 < M < 0.7$, $\bar{c}_{m_{\bar{h}}}$ is relatively constant (on the reduced frequency interval [0, 1]). For $M = 0.8$ a "wavy" pattern is very prominent in $\bar{c}_{m_{\bar{h}}}$. This wavy pattern reflects the slow upstream acoustic waves typical of high subsonic/transonic flow.[12] The wavy pattern persists in the aerodynamic moment up to and including $M = 0.9$. (The Mach numbers of 0.82, 0.84, 0.86, and 0.88 were also studied, but the results are not shown in Fig. 5.) At higher transonic numbers, from $M = 0.92$ to $M = 1.0$, the shock location is at the trailing edge of the chord, the flow over the airfoil chord is supersonic, and the wavy pattern is no longer present. (Not plotted here are curves for Mach numbers of 0.92, 0.94, 0.96, and 0.98 because they correspond very closely to $M = 1.0$ results shown in Fig. 5.) The oscillatory behavior of $\bar{c}_{m_{\bar{h}}}$ is attributed to the tendency of the fluid dynamic eigenspectrum to become less damped for transonic Mach numbers (see Ref. 1). Previous investigators have noted that computational waviness of this sort may be due to inadequate computational grid convergence.[13] However, it has also been known since the classical results of Landahl[14] that such waviness may arise from physical effects. The grid-convergence study previously discussed confirmed that the waviness in the present study is physical in origin.

Shown in Fig. 6a is a plot of the ratio of steady lift to pitch angle vs Mach number (for $\bar{\omega} = 0$) as obtained from this Euler flow model. For reference, the classical results as obtained from potential thin airfoil theory, $dc_l/d\alpha = 2\pi/\sqrt{(1-M)}$ at $\alpha = 0$, are also shown. The effects of airfoil profile (thickness) are clearly seen. Figure 6a presents the Euler flow model result for c_l divided by α (in radians) for $\alpha = 1$ rad. However, it is found that for the reduced frequency of zero, $\bar{\omega} = 0$, c_l/α is an erratic function of Mach number in the range $0.83 \leq M \leq 0.89$ for sufficiently small α (Fig. 6b). Note this is true even though for a fixed Mach number M, c_l/α is a smooth function of α (Fig. 6c). However, for the reduced frequencies of interest for the flutter boundaries studied here, $\bar{\omega} > 0.1$, these erratic variations in c_l/α are not present. To illustrate this, the case of Mach number $M = 0.868$ is considered. As one can see in Fig. 6b, at this value (marked by the vertical line) of Mach number M, there is a noticeable variation in the values of c_l/α with α when $\bar{\omega} = 0$. By contrast, as shown in Fig. 6c for $M = 0.868$, as the reduced frequency increases above $\bar{\omega} = 0.05$, the ratio of lift to pitch angle c_l/α is virtually constant with respect to α. Similar results were obtained for other Mach numbers, but are not presented here. It was also found that the degree of numerical smoothing in the CFD code could change the details of the results for lift at very small angles and very low reduced frequencies in the Mach number range where a rapid variation in lift occurs.

Finally, a comparison of aerodynamic transfer functions for this (NACA 64A010A) airfoil has been performed for $M = 0.8$ (Fig. 7). Lift $\bar{c}_{l_{\bar{\alpha}}}$ and moment $\bar{c}_{m_{\bar{\alpha}}}$ coefficients (both per radian) obtained by the present Euler code are compared to experimental values of Davis and Malcom[15] and other Euler calculations performed by Magnus[16] and Bendiksen and Kousen.[17] Also shown are the results of Ueda and Dowell[18] obtained by a describing function method based on LTRAN2 solver for transonic small-disturbance potential theory, as well as similar results by Isogai.[19] The results of Refs. 15–19 shown in Fig. 7 were taken from Figs. 3 and 4 of Ref. 17. The results obtained by the present Euler code were computed using one harmonic in the aerodynamic solution. No significant variations in lift and moment coefficients for the fundamental harmonic were observed when calculations were performed using two harmonics.

The several theoretical results shown in Fig. 7 for the lift and moment as a function of reduced frequency are on the whole consistent. However, there is some significant variation among them especially for phase angle, but less variation for magnitude. The trends predicted by the present theory and those from experiment are in encouragingly good agreement. Previous theoretical work provided data at relatively few reduced frequencies. The computational efficiency

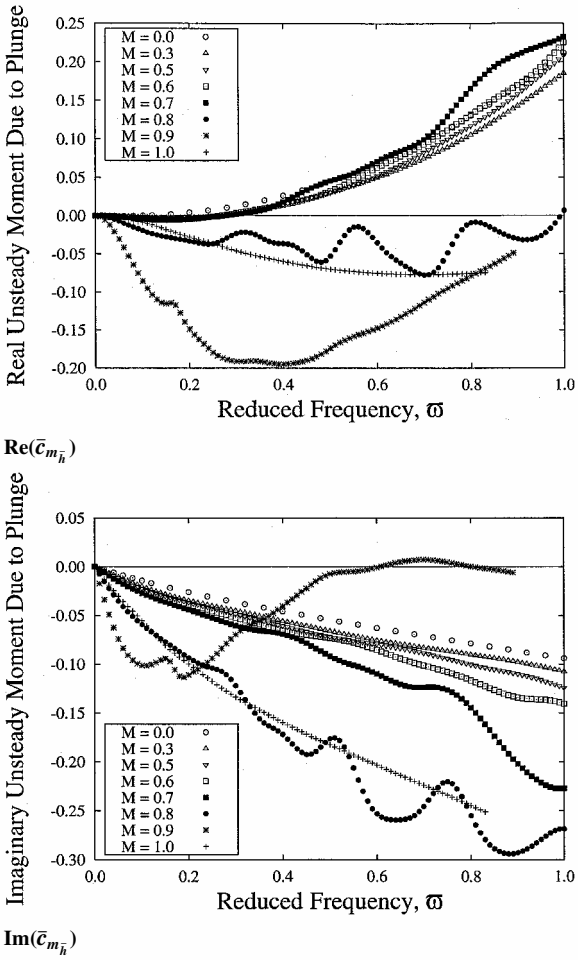

Fig. 5 Real and imaginary parts of the unsteady aerodynamic moment due to plunge motion vs reduced frequency $\bar{h} = 0.001$.

of the present theoretical method has allowed a more complete data set to be obtained.

Flutter

Rewriting the aeroelastic equations in terms of nondimensional variables yields

$$\left[-\bar{\omega}^2\begin{pmatrix}1 & x_\alpha\\ x_\alpha & r_\alpha^2\end{pmatrix}+\frac{4}{V^2}\begin{pmatrix}\omega_h^2/\omega_\alpha^2 & 0\\ 0 & r_\alpha^2\end{pmatrix}+\frac{4}{\pi\mu}\begin{pmatrix}\bar{c}_{l_{\bar{h}}} & \bar{c}_{l_{\bar{\alpha}}}\\ -2\bar{c}_{m_{\bar{h}}} & -2\bar{c}_{m_{\bar{\alpha}}}\end{pmatrix}\right]\begin{Bmatrix}\bar{h}\\ \bar{\alpha}\end{Bmatrix}=0 \tag{22}$$

In functional form and to emphasize the parameters involved, this equation can be written as

$$[\boldsymbol{F}(a, x_\alpha, r_\alpha,\ \text{geom},\ M, \bar{\omega}, \mu, \omega_h/\omega_\alpha, V)]\begin{Bmatrix}\bar{h}\\ \bar{\alpha}\end{Bmatrix}=0 \tag{23}$$

Even though the airfoil model considered has only two DOF, there are numerous structural and aerodynamic parameters that will affect the behavior of $\boldsymbol{F}$.

The elastic axis was placed at one-fifth of the chord ($a=-0.6$) and the airfoil radius of gyration and static unbalance were taken to be $r_\alpha^2=0.75$ and $x_\alpha=0.25$ to conform to the studies in Ref. 6. Aerodynamic coefficients $\bar{c}_{l_{\bar{h}}}$, $\bar{c}_{l_{\bar{\alpha}}}$, etc., were computed for various Mach numbers for reduced frequencies between zero and one. Thus, this leaves only the mass ratio μ, ratio of uncoupled frequencies ω_h/ω_α, and reduced velocity V as parameters to be considered in Eq. (23). Further fixing the value of either μ or ω_h/ω_α, normalizing the structural mode shape $\{\bar{h}, \bar{\alpha}\}$ to have a purely real-valued pitch

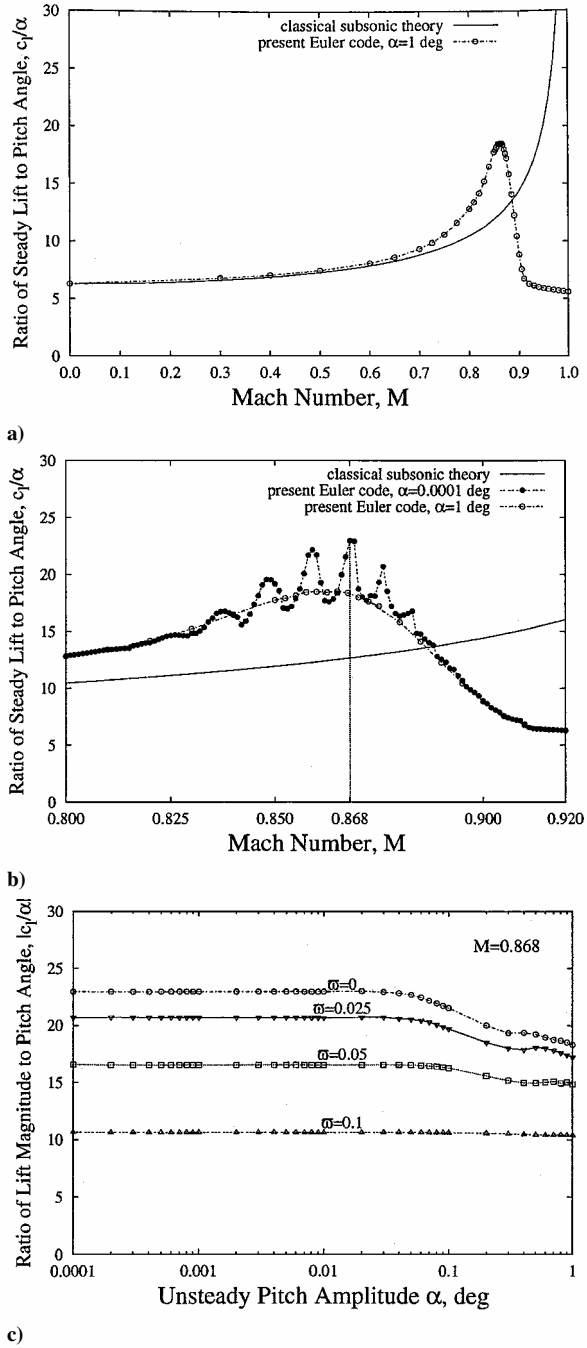

Fig. 6 Lift curve slope results: a) Ratio of steady lift to pitch angle c_l/α vs Mach number b) Ratio of steady lift to pitch angle c_l/α deduced for $\alpha = 0.0001$ and 1 rad vs Mach number and c) Ratio of lift magnitude to pitch angle $|c_l/\alpha|$ vs α for different reduced frequencies $0 \le \bar{\omega} \le 0.1$ at $M = 0.868$.

component (the bars on top of nondimensional amplitudes $\bar{h}$ and $\bar{\alpha}$ omitted in what follows)

$$[\boldsymbol{F}(\omega_h/\omega_\alpha \text{ or } \mu, V)]\begin{Bmatrix}h_r + ih_i\\ \alpha_r\end{Bmatrix}=0 \tag{24}$$

and setting the real and imaginary parts of the complex determinant to zero,

$$\det(\boldsymbol{F}) = (0, 0) \tag{25}$$

one obtains two real equations in $1/\mu$ or $\omega_h^2/\omega_\alpha^2$ and $1/V^2$ [see Eq. (22)]. The imaginary part of Eq. (25) provides a linear relation between the two unknowns, $1/\mu$ or $\omega_h^2/\omega_\alpha^2$ and $1/V^2$, and the real part of Eq. (25) then becomes a quadratic equation for $1/\mu$ or $\omega_h^2/\omega_\alpha^2$

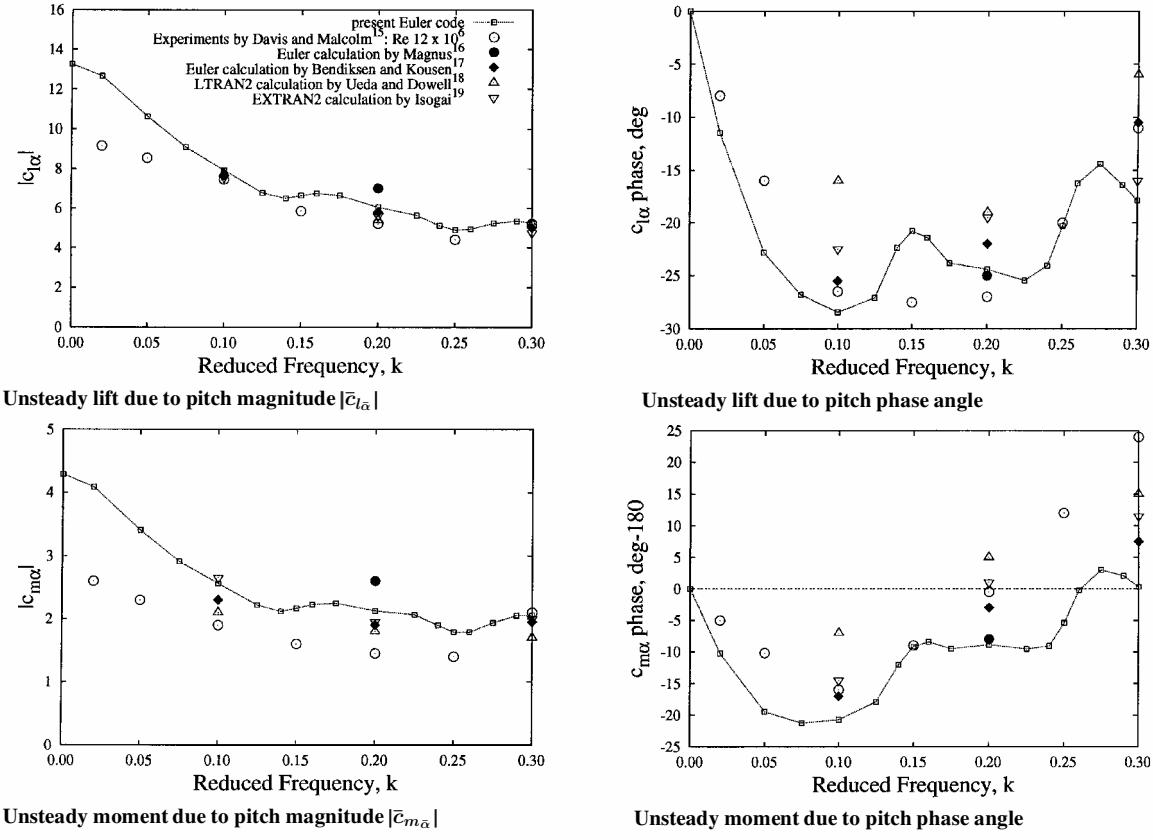

Unsteady lift due to pitch magnitude $|\bar{c}_{l\bar{\alpha}}|$

Unsteady lift due to pitch phase angle

Unsteady moment due to pitch magnitude $|\bar{c}_{m\bar{\alpha}}|$

Unsteady moment due to pitch phase angle

Fig. 7 Lift and leading-edge moment coefficients (both per radian) as functions of reduced frequency $k \equiv \omega b/U_\infty$ due to pitching ± 1 rad at the quarter-chord for $M = 0.8$.

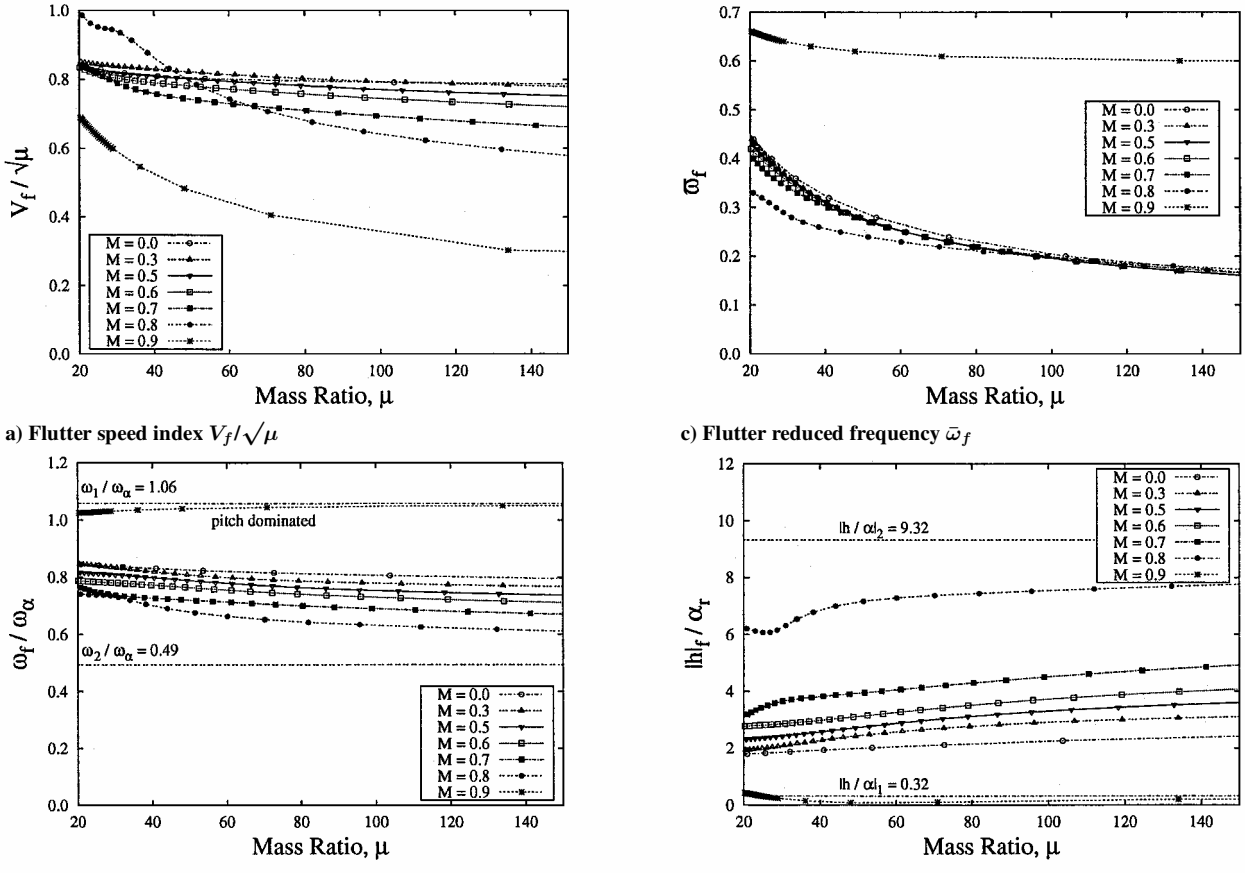

a) Flutter speed index $V_f/\sqrt{\mu}$

c) Flutter reduced frequency ϖ_f

b) Flutter frequency ratio ω_f/ω_α

d) Amplitude of flutter (aeroelastic) eigenvector $|h_f|/\alpha_r$

Fig. 8 Flutter behavior as function of mass ratio for $\omega_h/\omega_\alpha = 0.5$.

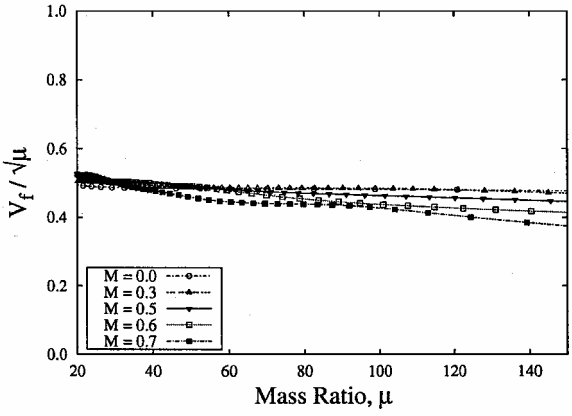

a) Flutter speed index $V_f/\sqrt{\mu}$

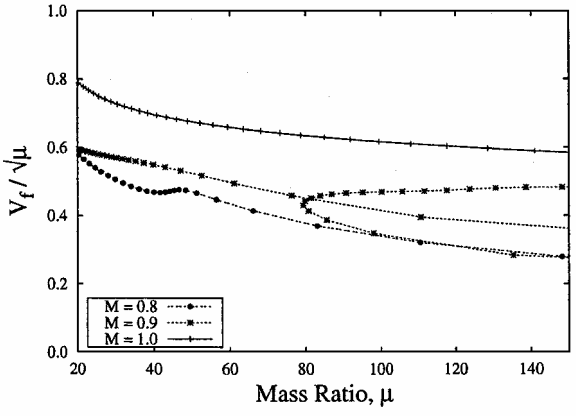

c) Flutter speed index $V_f/\sqrt{\mu}$

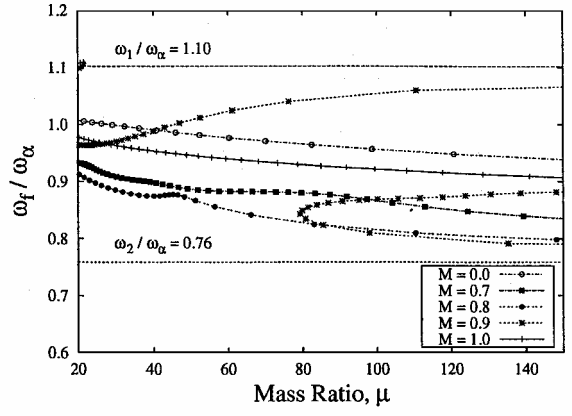

b) Flutter frequency ratio ω_f/ω_α

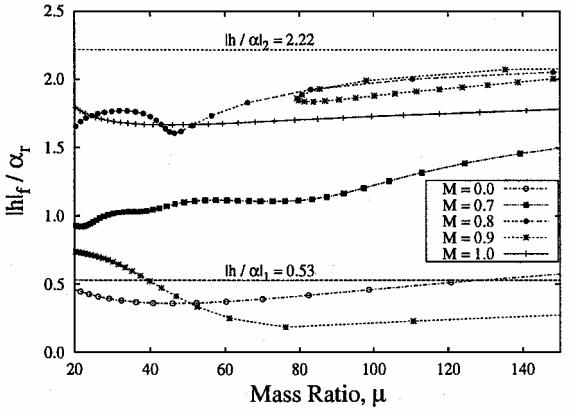

d) Amplitude of flutter (aeroelastic) eigenvector $|h_f|/\alpha_r$

Fig. 9 Flutter behavior as a function of the mass ratio for ω_h/ω_α = 0.8.

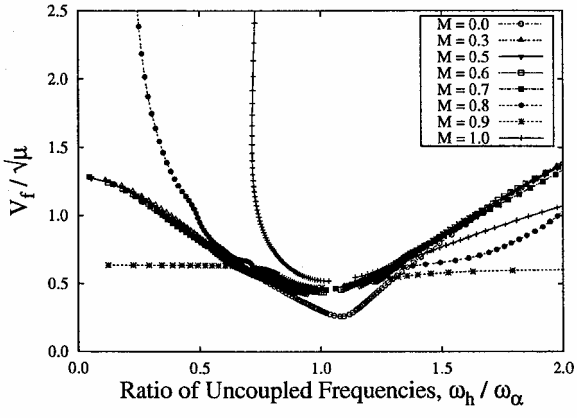

a) Flutter speed index $V_f/\sqrt{\mu}$

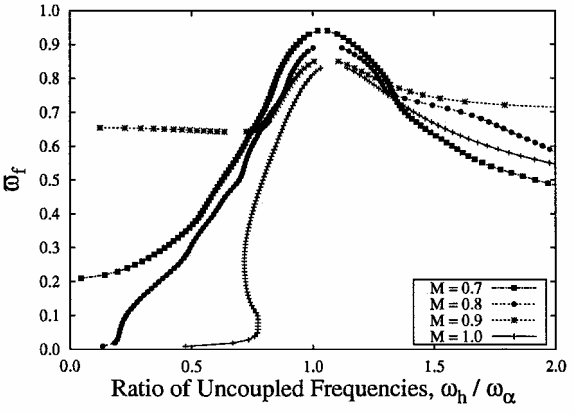

c) Flutter reduced frequency $\bar{\omega}_f$

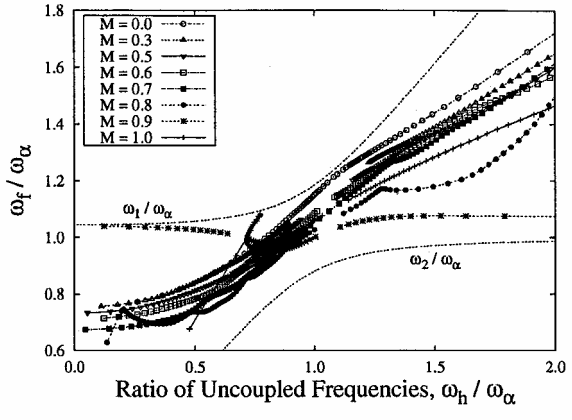

b) Flutter frequency ratio ω_f/ω_α

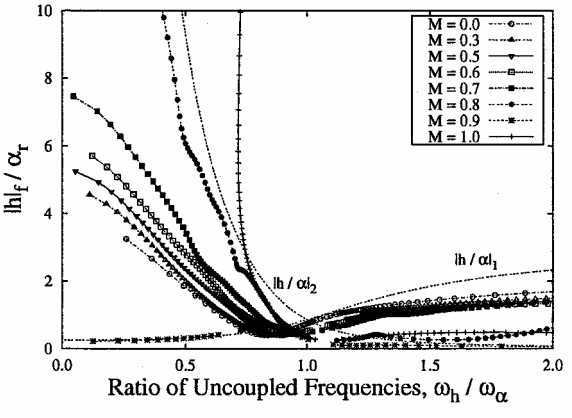

d) Amplitude of flutter (aeroelastic) eigenvector $|h_f|/\alpha_r$

Fig. 10 Flutter behavior as a function of the ratio of uncoupled frequencies for μ = 25.

that can be solved in closed form. The eigenvector, for example, $(h_r/\alpha_r, h_i/\alpha_r)$, at the flutter condition can then be determined from one of the two complex equations of Eq. (24).

Mass Ratio Effect

Dependence of the flutter boundaries (flutter speed index, flutter frequency, and eigenvector) on the mass ratio μ was investigated first. Two cases for the ratio of uncoupled frequencies are presented here: $\omega_h/\omega_\alpha = 0.5$ (Fig. 8) and $\omega_h/\omega_\alpha = 0.8$ (Fig. 9).

$\omega_h/\omega_\alpha = 0.5$

For $\omega_h/\omega_\alpha = 0.5$, the flutter speed index (Fig. 8a) is seen to be weakly dependent on μ for subsonic Mach numbers. For transonic Mach numbers of $M = 0.8$ and $M = 0.9$, the flutter speed index decreases with μ at a much higher rate. For $M = 1.0$, the flutter speed index becomes very large (well beyond the scale of the graph). Note that the flutter reduced frequency (Fig. 8c) for $M = 0.9$ is distinctly higher than for other Mach numbers. The flutter frequency (Fig. 8b) and flutter eigenvector (Fig. 8d) are also less sensitive to mass ratio at low subsonic Mach numbers with a more significant dependency occurring at higher subsonic and transonic Mach numbers. Coupled in vacuuo natural frequencies ω_1 and ω_2 were also computed for easy reference, and as can be seen in Fig. 8b, the flutter motion is pitch dominated for $M = 0.9$. One may also see this from Fig. 8d, where coupled in vacuuo eigenvectors $(h/\alpha)_1$ and $(h/\alpha)_2$ are indicated. The flutter eigenvector for $M = 0.9$ is essentially the same as $(h/\alpha)_1$, which corresponds to the pitch-dominated mode. This is an example of single-DOF flutter, but note the critical aeroelastic mode is a coupled natural mode, albeit one that is pitch dominated.

$\omega_h/\omega_\alpha = 0.8$

For $\omega_h/\omega_\alpha = 0.8$, the flutter speed index (Fig. 9a) is even more weakly dependent on μ for subsonic Mach numbers. In Fig. 9c, the flutter speed index behavior for transonic Mach numbers of $M = 0.8$, $M = 0.9$, and $M = 1.0$ is shown. As in the case of $\omega_h/\omega_\alpha = 0.5$, the flutter speed index for the transonic Mach numbers is more sensitive to μ than for the lower, subsonic Mach numbers. Moreover, for this frequency ratio, when $M = 0.9$, multiple flutter velocities occur for mass ratios $\mu \geq 80$. To determine the stability of the regions created by such multiple branches of flutter boundaries a root-loci analysis for fixed values of ω_h/ω_α and μ can be employed[8,20,21] using reduced-order aerodynamic models. However in this study, only flutter boundaries were determined. The flutter frequency (Fig. 9b) and flutter eigenvector (Fig. 9d) are distributed over the full range between coupled natural frequencies and eigenvectors, and none of Mach number cases appears to be primarily pitch or plunge dominated.

Ratio of Uncoupled Natural Frequencies Effect

Dependence of the flutter boundary on the ratio of uncoupled natural frequencies ω_h/ω_α is next investigated, and two mass ratios are considered: $\mu = 25$ (Figs. 10 and 11) and $\mu = 100$ (Fig. 12).

$\mu = 25$

For $\mu = 25$, the flutter speed index (Fig. 10a) has a minimum near $\omega_h/\omega_\alpha = 1$. For typical airfoils, ω_h/ω_α is usually between 0.2 and 0.8. In that range, the flutter speed index decreases steadily and is almost constant for Mach numbers less than 0.7. However, as can be seen and is well known, the flutter speed index becomes very sensitive to the Mach number for high subsonic or transonic conditions.

For a better understanding of how the flutter speed index results are obtained, one can show that the flutter reduced velocity may be expressed as

$$V_f^2 = \frac{d_1\left(\omega_h^2/\omega_\alpha^2\right) + d_2}{d_3} \tag{26}$$

where d_1, d_2, and d_3 are coefficients dependent on the reduced frequency. Equation (26) is obtained from the imaginary part of

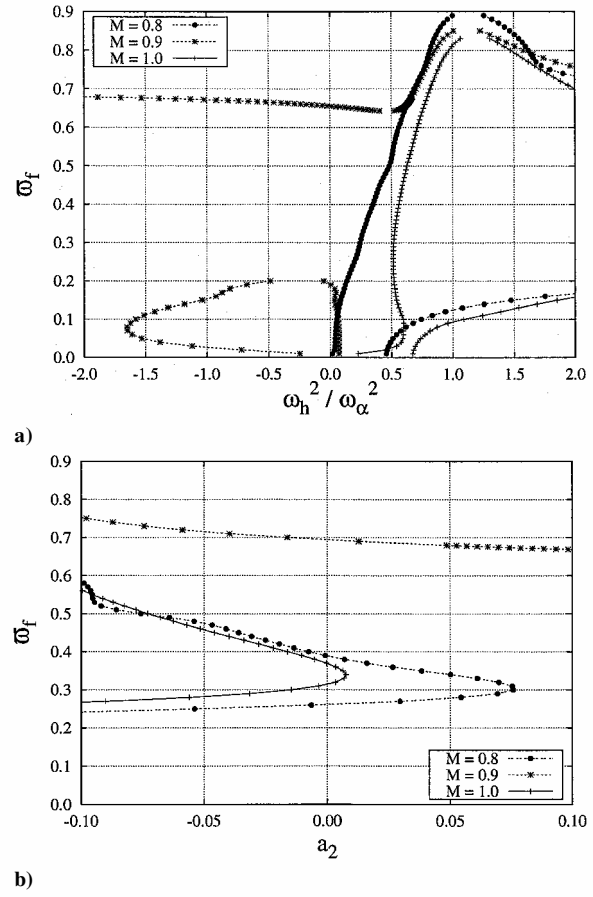

Fig. 11 Flutter reduced frequency $\bar{\omega}_f$ vs a) $\omega_h^2/\omega_\alpha^2$ and b) coefficient a_2 of $a_2(\omega_h^2/\omega_\alpha^2)^2 + a_1(\omega_h^2/\omega_\alpha^2) + a_0 = 0$ for $\mu = 25$.

Eq. (25). Substitution of Eq. (26) into the real part of Eq. (25) leads to a quadratic equation in $\omega_h^2/\omega_\alpha^2$,

$$a_2\left(\omega_h^2/\omega_\alpha^2\right)^2 + a_1\left(\omega_h^2/\omega_\alpha^2\right) + a_0 = 0 \tag{27}$$

with the roots given by

$$\left(\frac{\omega_h^2}{\omega_\alpha^2}\right)_{1,2} = \frac{-a_1 \pm \sqrt{a_1^2 - 4a_2a_0}}{2a_2} \tag{28}$$

where the coefficients a_i may also change the sign for different $\bar{\omega}$. Obviously, only positive real values of $\omega_h^2/\omega_\alpha^2$ in Eq. (28) have physical meaning. Moreover, only such values of $\omega_h^2/\omega_\alpha^2$ are kept for which V_f^2 in Eq. (26) is positive. Real roots of Eq. (28) are shown in Fig. 11a. When the coefficient a_2 passes through zero, branches of $\omega_h^2/\omega_\alpha^2$ asymptotically go to $\pm\infty$. The dependence of a_2 with respect to $\bar{\omega}_f$ is shown in Fig. 11b. For example, in Fig. 10c for $M = 0.9$, a_2 goes through zero at $\bar{\omega}_f \simeq 0.7$, which is when the branches of $\omega_h^2/\omega_\alpha^2$ go to $\pm\infty$ in Fig. 11a.

Note that the difference between the two coupled natural frequencies (ω_1 and ω_2 as indicated in Fig. 10b) is the smallest near $\omega_h/\omega_\alpha = 1$. This is likely responsible for the minimum in the flutter speed index in the vicinity of that point: The closer the coupled natural frequencies are initially, the more readily, when increasing velocity, "coalescence" or "merging frequency" flutter can occur (p. 112, Ref. 12).

$\mu = 100$

For $\mu = 100$, the flutter speed index (Figs. 12a and 12c) again has the tendency to have a minimum near $\omega_h/\omega_\alpha = 1$, especially so for subsonic Mach numbers (Fig. 12a). As in the case for $\mu = 25$, the flutter speed index is nearly constant with Mach number M for subsonic conditions. At higher transonic Mach numbers (Fig. 12c),

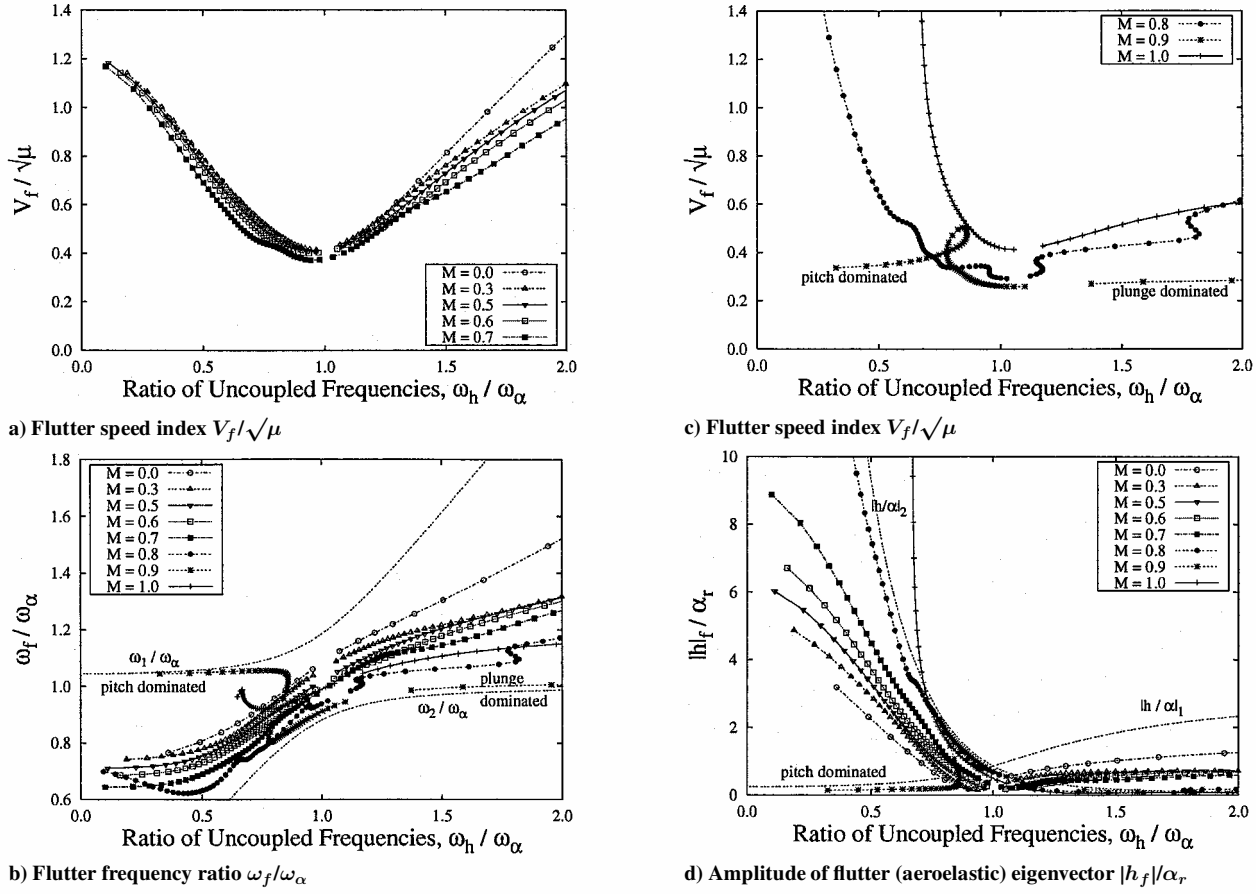

a) Flutter speed index $V_f/\sqrt{\mu}$

c) Flutter speed index $V_f/\sqrt{\mu}$

b) Flutter frequency ratio ω_f/ω_α

d) Amplitude of flutter (aeroelastic) eigenvector $|h_f|/\alpha_r$

Fig. 12 Flutter behavior as a function of ratio of uncoupled frequencies for μ = 100.

the flutter speed index becomes very sensitive to Mach number. This behavior is associated with the "transonic flutter dip." Also note that the flutter speed index can be a multivalued function of ω_h/ω_α for $M = 0.8$ and $M = 0.9$. Note that (Fig. 12b) the flutter frequency is very close to the coupled natural pitch frequency, ω_1/ω_α, for $M = 0.9$ (pitch-dominated motion). This is indicative of single-DOF flutter (p. 113, Ref. 12).

Mach Number Effect

The dependence of the flutter boundary on Mach number (Figs. 13 and 14) for the cases of $\mu = 25$ and 100 and $\omega_h/\omega_\alpha = 0.5$ and 0.8 is presented next.

$\omega_h/\omega_\alpha = 0.5$

Figure 13 shows the flutter boundary behavior vs Mach number for $\omega_h/\omega_\alpha = 0.5$. Squares represent the case of $\mu = 25$ and circles the case of $\mu = 100$. Note a rather weak dependence of the flutter boundaries on the mass ratio.

As the Mach number is increased past $M = 0.8$, a sharp drop in the flutter reduced frequency occurs. That is accompanied by a sharp increase in the flutter speed index. As the Mach number is increased further, another branch of flutter points appears. These low flutter speed index values correspond to the transonic flutter dip.

For an explanation to the abrupt change in flutter mode at $M = 0.82$ and $M = 0.91$, one may ask whether the steady flow shock position is changing and where the shock location is relative to the elastic axis and mode nodes.

The steady flow pressure contours for $M = 0.81$ and $M = 0.82$ did not show any significant changes in the pressure distribution. However, the situation is different for Mach numbers above $M = 0.9$. Here the location of the shock moves to the trailing edge as the Mach number is increased above $M = 0.9$. For $\omega_h/\omega_\alpha = 0.8$, the flutter behavior also changes in the viscinity of these Mach numbers. Note that in the Mach number range $0.82 < M < 0.92$ (Fig. 15) the position of the shock on the airfoil moves appreciably. To develop an improved understanding of the behavior of the flutter boundaries, one could perform a root locus analysis that would enable one to view the migration of the aeroelastic eigenvalues as a function of the nondimensional airspeed for each Mach number. Representative root locus analyses for transonic Mach numbers of similar airfoil models can be found in Refs. 8, 20, and 21. However, root loci have not been part of the present study.

The reduced flutter frequency behavior is shown in Fig. 13c. For subsonic and low transonic Mach numbers ($0 \le M \le 0.8$), $\bar{\omega}_f$ is much higher for the lower mass ratio ($\bar{\omega}_f \approx 0.4$) than for the higher mass ratio ($\bar{\omega}_f \approx 0.2$). At high transonic Mach numbers ($0.82 \le M < 0.92$), the flutter reduced frequency is about the same for either mass ratio.

The flutter (aeroelastic) eigenvector is shown in Fig. 13d and provides a possible explanation for the low flutter speed index values for the transonic dip Mach number region. In this range, the flutter mode becomes pitch dominated for both values of mass ratio. The flutter mode is markedly different from that for $M < 0.82$, for example.

$\omega_h/\omega_\alpha = 0.8$

The flutter speed index for $\omega_h/\omega_\alpha = 0.8$ is shown in Fig. 14a. For this rather high value of pitch to plunge frequency ratio, there is no transonic dip in the flutter speed index at the lower mass ratio. Moreover, the system appears to be more stable at the high transonic Mach numbers. For the higher mass ratio as the Mach number increases, the flutter velocity index reaches its minimum in the range $0.78 < M < 0.88$. The flutter mode then appears to change twice for even higher Mach numbers. Contrary to the results for $\omega_h/\omega_\alpha = 0.5$, here the flutter frequency shown in Fig. 14b is not very close to either the pitch- or plunge-coupled natural frequency. Thus, the flutter mode (Fig. 14d) is not a single-DOF flutter motion, but rather a combined pitch–plunge motion.

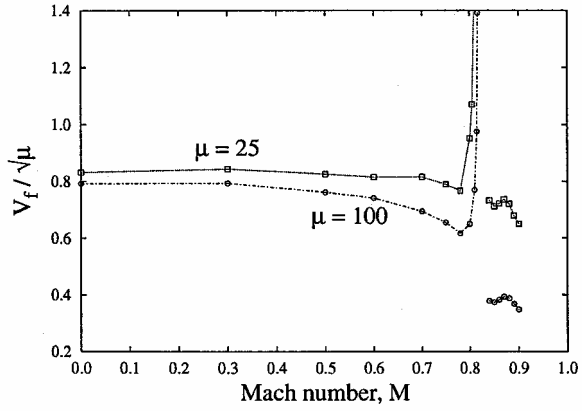

a) Flutter speed index $V_f/\sqrt{\mu}$

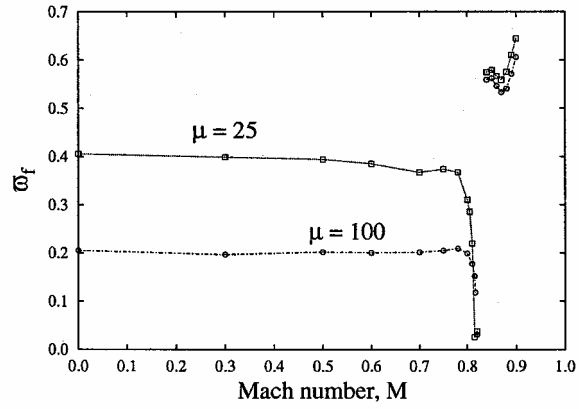

c) Flutter reduced frequency $\bar{\omega}_f$

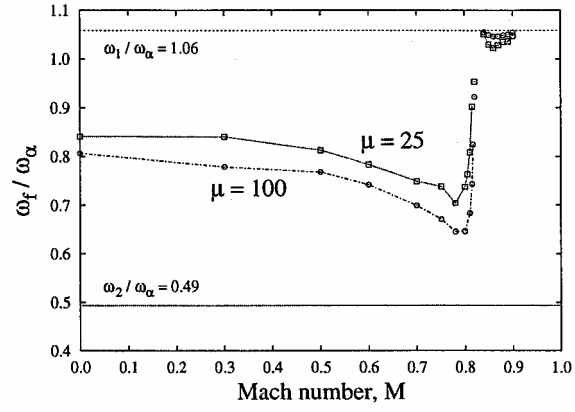

b) Flutter frequency ratio ω_f/ω_α

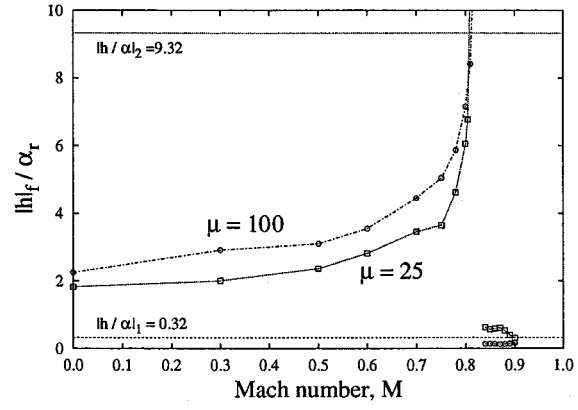

d) Amplitude of flutter (aeroelastic) eigenvector $|h_f|/\alpha_r$

Fig. 13 Flutter behavior as function of Mach number for $\omega_h/\omega_\alpha = 0.5$ and $\mu = 25$ and 100.

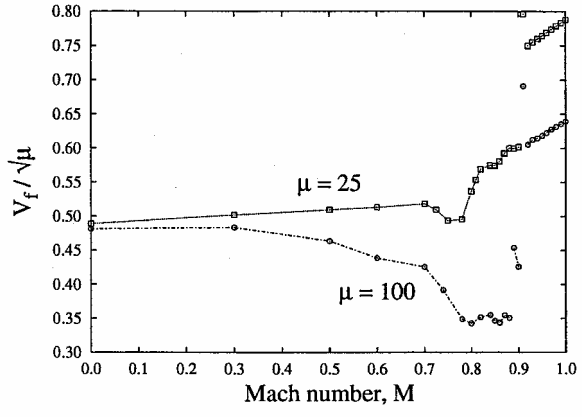

a) Flutter speed index $V_f/\sqrt{\mu}$

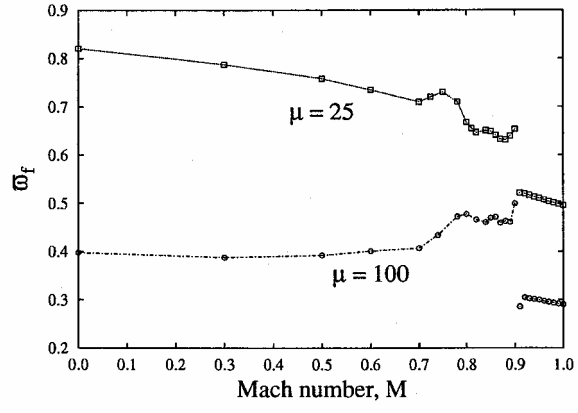

c) Flutter reduced frequency $\bar{\omega}_f$

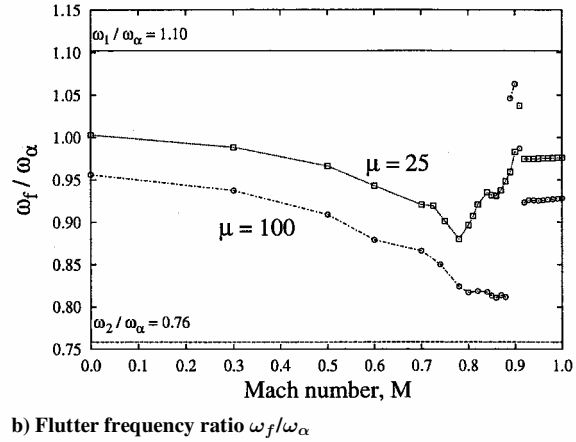

b) Flutter frequency ratio ω_f/ω_α

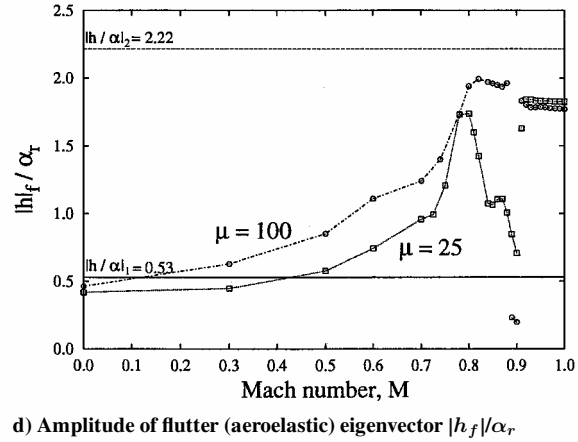

d) Amplitude of flutter (aeroelastic) eigenvector $|h_f|/\alpha_r$

Fig. 14 Flutter behavior as function of Mach number for $\omega_h/\omega_\alpha = 0.8$ and $\mu = 25$ and 100.

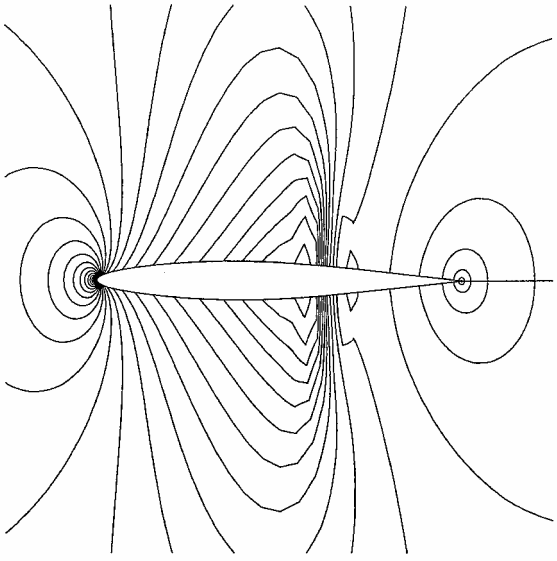

$M = 0.82$

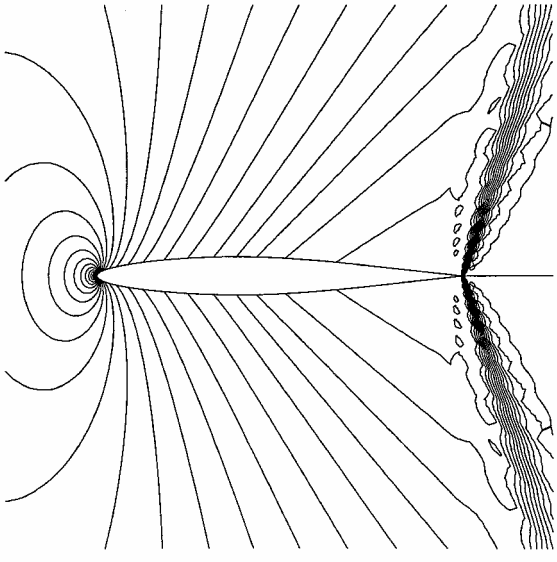

$M = 0.92$

Fig. 15 Steady flow pressure contours.

Conclusions

Using a state of the art Euler-based time-linearized aerodynamic code, an investigation is presented of how structural and aerodynamic parameters including freestream (transonic) Mach number affect flutter and LCO characteristics of a typical two-DOF airfoil configuration. Convergence of the CFD code with respect to grid spacing and computational domain size was also considered.

The following conclusions have been drawn.

1) When the dependence of the flutter on the mass ratio μ was examined, it was found that the flutter variables, that is, reduced velocity, frequency, and structural eigenmode, vary little with μ, especially for subsonic Mach numbers.

2) As expected, a study of the effect of the ratio of uncoupled natural frequencies ω_h/ω_α determined that flutter reduced velocities have a minimum near $\omega_h/\omega_\alpha \approx 1$. Multiple values of the flutter velocity can occur at high transonic Mach numbers for some ω_h/ω_α.

3) Most significantly perhaps, it was demonstrated that flutter solutions are very sensitive to Mach number especially in the transonic range. When the frequency and the mass ratios are depended on, there may or may not be sudden and significant changes, for example, the transonic dip, in the flutter reduced velocity and the type of flutter motion as the Mach number is varied.

4) Finally, note that viscous effects may be important.[22] It has been our experience that when the aerodynamic flow is attached an inviscid analysis is adequate, but for separated flows, a viscous analysis is required.

An extensive parameter analyses of an airfoil aeroelastic configuration has been achieved using a highly efficient time linearized CFD computational technique. Correlation with experiment remains an open challenge; however, a comparison of results from our CFD model with results from an unsteady aerodynamic experiment by Davis and Malcom[15] for lift and moment shows encouraging agreement.

Acknowledgments

This work was supported by the Air Force Office of Scientific Research Grant "Computation of Limit Cycle Oscillations in Support of Flight Flutter Testing." Len Sakel and Charles Denegri are the program managers.

References

[1]Dowell, E. H., and Hall, K. C., "Modeling of Fluid–Structure Interaction," *Annual Review of Fluid Mechanics*, Vol. 33, 2001, pp. 445–490.

[2]Vepa, R., "On the Use of Padé Approximates to Represent Unsteady Aerodynamic Loads for Arbitrarily Small Motions of Wings," AIAA Paper 76-17, Jan. 1976.

[3]Karpel, M., "Design for Active Flutter Suppression and Gust Alleviation Using State-Space Aeroelastic Modeling," *Journal of Aircraft*, Vol. 19, No. 3, 1982, pp. 221–227.

[4]Raveh, D. E., Levy, Y., and Karpel, M., "Aircraft Aeroelastic Analysis and Design Using CFD-Based Unsteady Loads," *41st Structures, Structural Dynamics, and Materials Conference and Exhibit*, AIAA Paper 2000-1325, Reston, VA, 2000.

[5]Hall, K. C., Thomas, J. P., and Clark, W. S., "Computation of Unsteady Nonlinear Flows in Cascades Using a Harmonic Balance Technique," *AIAA Journal*, Vol. 40, No. 5, 2002, pp. 879–886.

[6]Thomas, J. P., Dowell, E. H., and Hall, K. C., "Nonlinear Inviscid Aerodynamic Effects on Transonic Divergence, Flutter, and Limit-Cycle Oscillations," *AIAA Journal*, Vol. 40, No. 4, 2002, pp. 638–646.

[7]Kholodar, D. B., Thomas, J. P., Dowell, E. H., and Hall, K. C., "A Parameter Study of Transonic Airfoil Flutter and Limit-Cycle Oscillation Behavior," *43rd Structures, Structural Dynamics, and Materials Conference and Exhibit*, AIAA Paper 2002-1211, Denver, CO, 2002.

[8]Hall, K. C., Thomas, J. P., and Dowell, E. H., "Proper Orthogonal Decomposition Technique for Transonic Unsteady Aerodynamic Flows," *AIAA Journal*, Vol. 38, No. 10, 2000, pp. 1853–1862.

[9]Ni, R., "A Multiple Grid Scheme for Solving the Euler Equations," *AIAA Journal*, Vol. 20, No. 11, 1982, pp. 1565–1571.

[10]Saxor, A. P., "A Numerical Analysis of 3-D Inviscid Stator/Rotor Interactions Using Non-Reflecting Boundary Conditions," Gas Turbine Lab. Rept. 209, Massachusetts Inst. of Technology, Cambridge, MA, March 1992.

[11]Kholodar, D. B., "Aeroelastic Response of an Airfoil with Structural and Aerodynamic Nonlinearities," Ph.D. Dissertation, Dept. of Mechanical Engineering and Material Science, Duke Univ., Durham, NC, May 2002.

[12]Dowell, E. H., Crawley, E. F., Curtiss, Jr., H. C., Scanlan, R. H., and Sisto, F., *A Modern Course in Aeroelasticity*, edited by E. H. Dowell, Kluwer Academic, Norwell, MA, 1995, pp. 12, 113.

[13]Seidel, D. A., Bennett, R. M., and Whitlow, W., Jr., "An Exploratory Study of Finite Difference Grids for Transonic Unsteady Aerodynamics," NASA TM-84583, 1982.

[14]Landahl, M., *Unsteady Transonic Flow*, Pergamon, Oxford, 1961.

[15]Davis, S. N., and Malcom, G. N., "Transonic Shock-Wave/Boundary-Layer Interactions on an Oscillating Airfoil," *AIAA Journal*, Vol. 18, No. 11, 1980, pp. 1306–1312.

[16]Magnus, R. J., "Computational Research on Inviscid, Unsteady, Transonic Flow Over Airfoils," Office of Naval Research, Rept. ONR CASCD/LVP 77-010, 1977.

[17]Bendiksen, O. O., and Kousen, K. A., "Transonic Flutter Analysis Using the Euler Equations," *AIAA Dynamics Specialist Conference*, AIAA Paper 87-0911-CP, April 1987.

[18]Ueda, T., and Dowell, E. H., "Flutter Analysis Using Nonlinear Aerodynamic Forces," *Journal of Aircraft*, Vol. 21, No. 2, 1984, pp. 101–109.

[19]Isogai, K., "Numerical Study of Transonic Flutter of a Two-Dimensional Airfoil," NAL TR-617T, National Aerospace Inst., Tokyo, Japan, 1980.

[20]Thomas, J. P., Dowell, E. H., and Hall, K. C. "Transonic Limit-Cycle Oscillation Analysis Using Reduced Order Aerodynamic Models," *42nd Structures, Structural Dynamics, and Materials Conference and Exhibit*, AIAA Paper 2001-1212, Seattle, WA, 2001.

[21]Florea, R., Hall, K. C., and Dowell, E. H., "Eigenmode Analysis and Reduced-Order Modeling of Unsteady Transonic Potential Flow Around Airfoils," *Journal of Aircraft*, Vol. 37, No. 3, 2000, pp. 454–462.